



Article

Atomic Layer Deposition of Mixed-Layered Aurivillius Phase on TiO₂ Nanotubes: Synthesis, Characterization and Photoelectrocatalytic Properties

Farid Orudzhev ^{1,*}, Shikhgasan Ramazanov ¹, Dinara Sobola ^{1,2,3}, Abdugelim Isaev ¹, Chuanyi Wang ⁴, Asiyat Magomedova ¹, Makhmud Kadiev ¹ and Kasinathan Kaviyarasu ^{5,6}

¹ Department of Inorganic Chemistry and Chemical Ecology, Dagestan State University, st. M. Gadjieva 43-a, Dagestan Republic, 367015 Makhachkala, Russia; ramazanv@mail.ru (S.R.); sobola@vutbr.cz (D.S.); abdul-77@yandex.ru (A.I.); asiyat_magomedova1996@mail.ru (A.M.); k.mahmud@yandex.ru (M.K.)

² Department of Physics, Faculty of Electrical Engineering and Communication, Brno University of Technology, Technická 2848/8, 61600 Brno, Czech Republic

³ Central European Institute of Technology BUT, Purkyňova 123, 61200 Brno, Czech Republic

⁴ School of Environmental Science and Engineering, Shaanxi University of Science & Technology, Xi'an 710021, China; wangchuanyi@sust.edu.cn

⁵ UNESCO-UNISA Africa Chair in Nanoscience's/Nanotechnology Laboratories, College of Graduate Studies, University of South Africa (UNISA), Muckleneuk Ridge, P.O. Box 392, Pretoria 0003, South Africa; Kasinathankaviyarasu@gmail.com

⁶ Nanosciences African Network (NANOAFNET), Materials Research Group (MRG), iThemba LABS-National Research Foundation (NRF), 1 Old Faure Road, 7129, P.O. Box 722, Somerset West 8000, South Africa

* Correspondence: ff.orudzhev@dgu.ru; Tel.: +7-928-866-26-22

Received: 3 October 2020; Accepted: 30 October 2020; Published: 2 November 2020



Abstract: For the first time, one-dimensional phase-modulated structures consisting of two different layered Aurivillius phases with alternating five and six perovskite-like layers were obtained by atomic layer deposition (ALD) on the surface of TiO₂ nanotubes (Nt). It was shown that the use of vertically oriented TiO₂ Nt as the substrate and the ALD technology of a two-layer Bi₂O₃-FeO_x sandwich-structure make it possible to obtain a layered structure due to self-organization during annealing. A detailed study by scanning electron microscopy (SEM) and transmission electron microscopy (TEM) showed that the coating is conformal. Raman spectroscopic analysis indicated the structure of the layered Aurivillius phases. Transient photocurrent responses under Ultraviolet-Visible (UV-Vis) light irradiation show that the ALD coating benefits the efficiency of photon excitation of electrons. The results of the photoelectrocatalytic experiments (PEC) with methyl orange degradation as a model demonstrate the significant potential of the synthesized structure as a photocatalyst. Photoluminescent measurement showed a decrease in the probability of recombination of photogenerated electron-hole pairs for ALD-coated TiO₂ Nt, which demonstrates the high potential of these structures for use in photocatalytic and photoelectrochemical applications.

Keywords: atomic layer deposition; photocatalysis; photoelectrocatalysis; TiO₂ nanotubes; Aurivillius phase; layered perovskite

1. Introduction

It is known that the Aurivillius phases of the Bi₄Ti₃O₁₂-BiFeO₃ (BFTO) system combine ferroelectric, semiconductor and ferromagnetic properties and that they are potentially attractive for a large number of applications [1,2]. These oxides have a layered perovskite structure where fluorite-like layers (Bi₂O₂)²⁺ alternate with perovskite-like layers (Bi_{n+1}Fe_{n-3}Ti₃O_{3n+1})²⁻. The index n indicates the number of

perovskite-like layers in one block and can be an integer or a fractional value [3]. Fractional values of n correspond to multilayer structures that contain alternating perovskite-like blocks of different layers and appear due to the fact that the Aurivillius phase system is inclined to structural disorder [4,5]. The compounds of the Aurivillius phases have been mostly studied as bulk crystals and ceramics [6,7] and there are only few reports on the synthesis and study of thin films [4]. Preparation of multicomponent oxides by the atomic layer deposition (ALD) method is a difficult task because the search for optimal growth parameters is time-consuming and requires a large number of experiments and resources. Bismuth-containing oxides with layered structures, especially representatives of the Aurivillius family, have attracted increasing attention in recent years as visible-light-active photocatalysts [8–10]. The presence of Bi increases the probability of absorption of visible light, shifting the edge of the valence band (VB) due to the hybridization of Bi 6s with the O 2p orbital and contributes to the high mobility of photogenerated holes [10].

The highly oriented arrays of TiO₂ nanotubes (Nt) have long demonstrated excellent photovoltaic and photocatalytic properties due to their unique morphology, high specific surface area and unidirectional charge transfer, resulting in small losses at grain boundaries due to recombination [11]. A recent review article [12] examined, in detail, the works in which ALD technology was used for the functionalization of TiO₂ Nt with other materials to improve their physicochemical properties, such as light absorption, separation of photogenerated electron-hole pairs, photocatalytic and photoelectrocatalytic properties, chemical, thermal and mechanical stability and others.

In this work, for the first time, we report on ALD synthesis of the mixed-layer structure of Aurivillius on a substrate of TiO₂ Nt, using them as an alternative to ALD cycles associated with titanium-containing precursors. Thus, we simplified the ALD technology of multicomponent oxide systems and obtained a structure with a more advanced surface. This approach provides opportunities for new applications in relevant fields, such as photocatalytic decomposition of pollutants and photoelectrochemical water splitting.

2. Materials and Methods

2.1. Synthesis Procedure

The film was grown in an ALDCERAM ML-200 (ALDCERAM, LLC, Boulder, CO, USA) atomic layer deposition reactor. The substrate used was TiO₂ Nt on Ti foil, prepared as described in the work [13]. The details of the synthesis procedure were described by us in our previous work [14,15], where the Bi-Fe-O phase was synthesized on the surface of highly oriented pyrolytic graphite (HOPG). In this work, the other number of cycles was used at the ALD process (Bi₂O₃ (90 cycles)-FeO_x (90 cycles)). The TiO₂/Ti structure was used as the substrate and the samples were annealed at 660 °C in air for one hour. The source of bismuth was Bi(mmp)₃ precursor (its chemical formula is C₁₅H₃₃O₆Bi) (Sigma-Aldrich, Schnelldorf, Germany). The ferrocene-Fe(Cp)₂ was used as an iron-containing organometallic precursor (its chemical formula is Fe(C₅H₅)₂) (Sigma-Aldrich, Schnelldorf, Germany).

2.2. Characterizations

Characterization of the obtained heterostructures was performed using scanning electron microscopy (SEM) with the scanning electron microscope Magellan (Thermo Fisher Scientific, Hillsboro, OR, USA) and transmission electron microscopy (TEM) with TITAN 80-300 (FEI, Fremont, CA, USA). X-ray diffraction (XRD) studies were done using an Empyrean PANalytical X-ray diffractometer (Almelo, Netherlands) in the radiation of a copper anode with a nickel filter, with radiation wavelength $\lambda(\text{CuK}\alpha) = 0.154051$ nm. Data processing was performed using the High Score Plus application program, included in the instrument software, and the diffraction database ICSD (PDF-2). Additional study of the surface composition was carried out by an AXIS SupraTM X-ray photoelectron spectrometer (XPS) (Kratos Analytical Ltd., Manchester, UK). The data were processed by CasaXPS v.2.3.23 software (Casa Software Ltd., Wilmslow, UK). Raman spectra were examined by a Laser Raman 3D scanning confocal

microscope (Ntegra Spectra, Moscow, Russia) using a green laser (532 nm) with a spot size of 1 μm and a resolution of 0.5 cm^{-1} . Photoluminescence spectra were recorded by a Lyumakhrom Fluorat-02 panorama spectrofluorometer (St. Petersburg, Russia) with a 320-nm wavelength of exciting radiation.

Diffuse reflection spectra were measured by a Shimadzu UV-3600 (Kyoto, Japan) spectrophotometer with an LISR-3100 integrating sphere in the coordinates $F(R) = f(\lambda, \text{nm})$, where $F(R)$ is the Kubelka–Munk function (denoted in the text as α). We used the method of the Tauc curve plot to determine the band gap by conversion of the optical absorption spectra using the absorption coefficient (α) and photon energy ($h\nu$), calculated considering the wavelengths: $h\nu = 1240/\lambda$. The band gap energy was determined by extrapolation of the linear area of the dependence of $(\alpha h\nu)^n$ on $(h\nu)$ to the zero value of the absorption coefficient, where n is equal $\frac{1}{2}$ in the case of indirect and n is equal 2 in the case of direct inter-band transition. Urbach energy values (EU) were calculated by inverse slope of the dependence of $\ln\alpha$ on $h\nu$.

2.3. Photoelectrochemical Measurement

Transient photocurrent responses under Ultraviolet–Visible (UV-Vis) light irradiation were studied by the potentiostat-galvanostat IPC-Pro MF (St. Petersburg, Russia). A saturated silver chloride Ag-AgCl electrode was used as a reference electrode. Platinum electrode was used as the counter electrode. The synthesized samples of pure and ALD-coated TiO_2 Nt were the working electrodes. The area of the working electrode was 0.25 cm^2 . The distance between the electrodes was 2 cm. During the photoelectrocatalytic experiments (PEC), a solution of freshly prepared methyl orange (MO) dye (30 mL of 5 mg/L concentration) with 0.1 M Na_2SO_4 was irradiated by UV-Vis light in quartz cell. The experiment was carried out without a voltage offset. The light source was a 250 W discharge mercury vapor lamp with a preliminary removed phosphor layer and a 365 nm main wavelength. The emission spectrum is given in Figure S1. To study the kinetics of the PEC process, the absorption spectra were measured every 10 min on a Specord 210 plus spectrophotometer (Analytik Jena, Jena, Germany) with a 1 nm step and 10 nm/s speed. After this, the solution was returned to the cell and the process continued.

3. Results

The intense volatilization of bismuth is one of the fundamental problems in the synthesis of bismuth-containing ternary compositions [16]. Therefore, we decided to use the technology for producing a two-layer sandwich structure from Bi_2O_3 (90 cycles)- FeO_x (90 cycles), in contrast to the previously proposed homogenous mix technology [17]. Considering the problem of volatilization, we synthesized the first layer of crystallized Bi_2O_3 . As has been previously shown [18], the alpha phase of bismuth oxide crystallizes already during the growth at 250 °C. The region of $\text{Bi}_2\text{O}_3/\text{TiO}_2$ is formed at the interface with nanotubes. According to our assumption, the next deposited FeO_x layer should limit the volatilization of bismuth during further annealing, since the chemical reaction will occur at active bismuth diffusion through the FeO_x layer. Figure 1 shows a scheme of the processes during ALD and subsequent annealing of the sample.

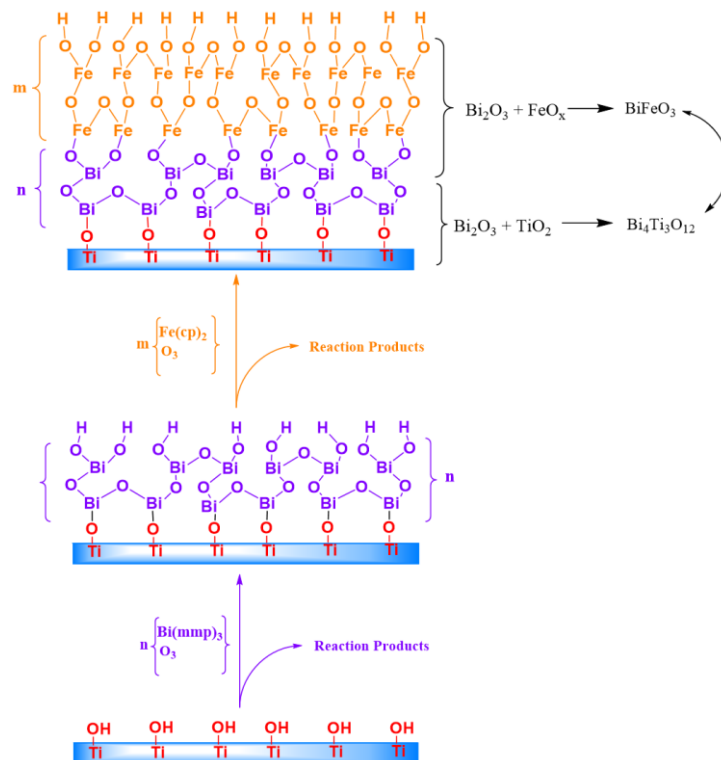


Figure 1. Schematic process of atomic layer deposition (ALD) Aurivillius phase formation.

The compounds of the Aurivillius phases are formed in the Bi₂O₃-TiO₂ composition at $n(\text{Bi})/n(\text{Ti}) > 1$ [19]. The processes of the compounds' formation at the phase boundary between Bi₂O₃ and TiO₂ in the TiO₂-Bi₂O₃-TiO₂ sandwich composition were studied by Lu et al. [20]. The authors concluded that first, a stable compound, Bi₄Ti₃O₁₂, is formed in the Bi₂O₃ layer due to diffusion of titanium. In addition, the annealing temperature of 660 °C is close to the melting point of the phase to γ -Bi₂O₃ ($T_m \approx 550\text{--}630$ °C). It causes significant increasing in the mass-transfer rate and initiation of chemical reactions, which also contributes to reaction 1.

The intensive mass transfer of bismuth oxide along the surface of the growing film during annealing of the sample leads to a solid-phase reaction in the near-surface region:



Due to mass-transfer, the reaction in the Bi₂O₃-FeO_x region could be described by Equation 2:



During annealing, the interaction of two phases, BiFeO₃-Bi₄Ti₃O₁₂, as shown in Figure 1, leads to the formation of the layered structure of the Aurivillius phase. The number of layers in this structure is due to the presence of BiFeO₃ in the perovskite-like block [2]. Figure 2 shows SEM images of the surface of TiO₂ Nt before and after the deposition process.

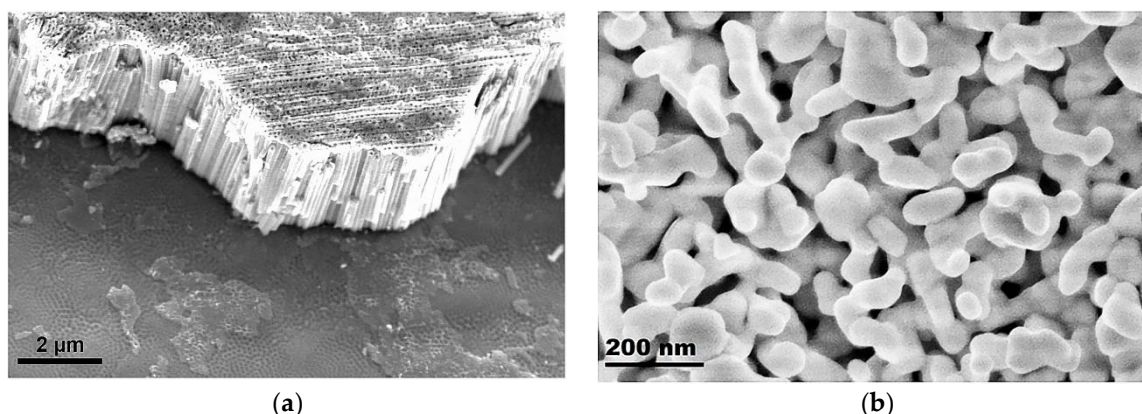


Figure 2. Scanning electron microscopy (SEM) images of (a) pure and (b) ALD-coated TiO₂ nanotubes (Nt) on Ti foil.

As can be seen from Figure 2a, the substrate surface before ALD is coated with an array of vertically oriented TiO₂ Nt with a diameter of about 100 nm and a length of about 2 μm. Figure 2b demonstrates the surface of nanotubes after ALD of Bi₂O₃-FeO_x. It can be seen that the surface of the nanotubes is coated with an inhomogeneous layer of nanostructures with a diameter of about 100 nm. There are pores up to 50 nm wide through which the surface of the nanotubes is visible. TEM studies were carried out for a more detailed characterization of the coating (Figure 3). A TEM image of a single ALD-coated TiO₂ Nt is shown in Figure 3a. It is shown that a single nanotube is uniformly covered with a film about 20 nm thick. The film contains nanocrystals with grain sizes of 10–15 nm (dark areas) together with the presence of an amorphous phase (light areas). Experimental data on the formation kinetics of the layered perovskite-like compounds in the BFTO system showed that the Aurivillius phase begins to form at 600 °C [21]. Figure 3b shows an enlarged area near the nanotube–film interface. It is shown that a complex layered structure is formed after annealing at 660 °C in the nanotube–film interface, which is typical to the Aurivillius phases. The crystal lattice of all Aurivillius phases consists of perovskite-like layers (A_{n-1}B_nO_{3n+1})²⁻, which alternate with (Bi₂O₂)²⁺ bismuth-oxygen layers (Figure 3c). Fourier analysis of the region with a high resolution (Figure 3c,d) allowed to visualize one-dimensional (1D) phase-modulated structures consisting of two different layered Aurivillius phases with alternating the number of five and six perovskite-like layers (Figure 3c). Modulation of the interface in the periodically laid structures was previously reported; however, it was usually carried out by doping various positions of the structure with alkaline-earth or rare-earth metal ions [22,23]. The transition between layers with a different number of blocks is accompanied by stacking defects in the (Bi₂O₂)²⁺ layer. Such interfaces between 5- and 6-layer blocks can lead to complex deformations and distortions. The perovskite structure remains in this case and regular lattice distortions appear in certain regions without changing the general layout and forming regions with morphotropic phase transitions [24]. Such regions are probably associated with the substitution of Fe³⁺ ions in a narrow range of 0.58–0.65 for Ti⁴⁺ ions in octahedral cells [25]. Kikuchi [26] also explains the formation of such regions by the 6% difference in the ionic radii of iron and titanium, which leads to a shift of these ions relative to (Bi₂O₂)²⁺ layers.

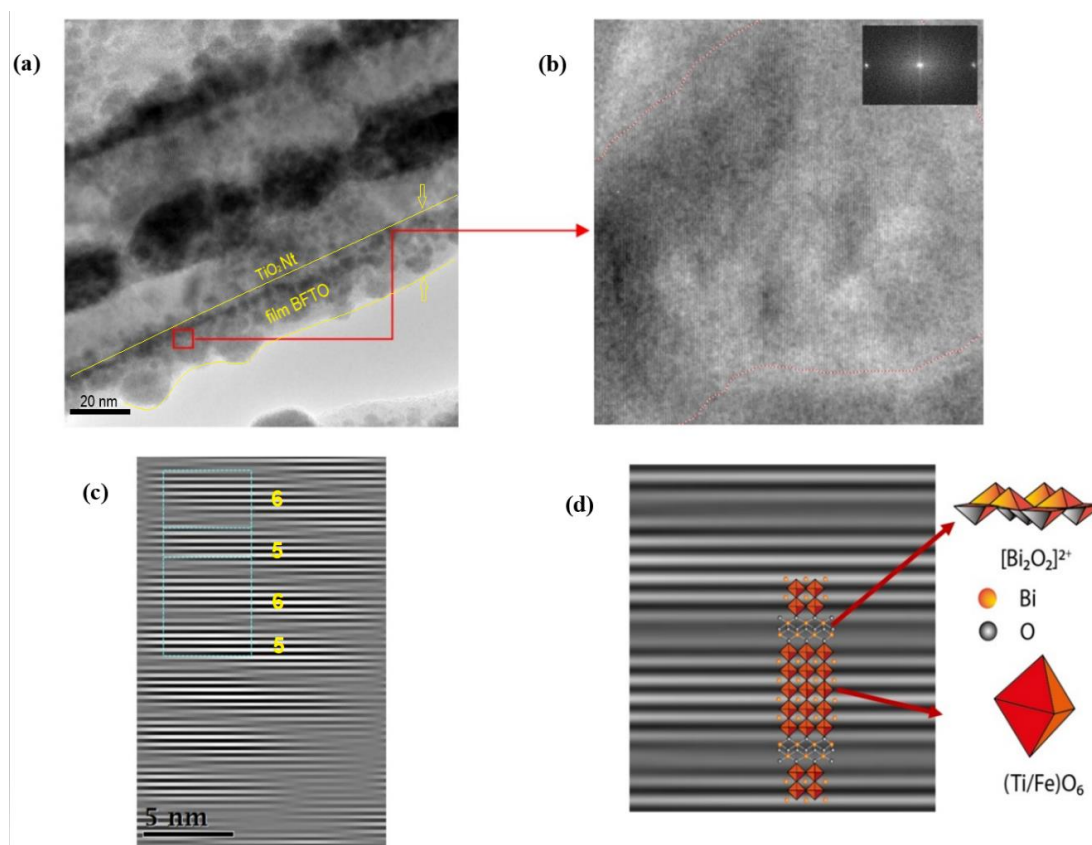


Figure 3. Transmission electron microscopy (TEM) analysis: (a) image of an ALD-coated single TiO₂ Nt, (b) enlarged area (7 × 7 nm²) near the nanotube–film interface where the layered structure is visualized and (c,d) Fourier masked micrographs of the layered structure region.

Typical XRD patterns of the pure and ALD-coated TiO₂ Nt grown on Ti substrate are shown in Figure 4. It is revealed that the pure TiO₂ Nt exhibit a phase of anatase (ICSD reference code: 98-015-4603) and Ti (ICSD reference code: 98-065-3275). The overlap of XRD peaks occurred because of large amount of phases in the obtained structure. After annealing at 660 °C, an initial phase of anatase partially transformed into the rutile phase with the characteristic diffraction peak at $2\theta = 27.7^\circ$ (110) [27]. The anatase/rutile ratio in ALD-coated TiO₂ Nt calculated using Equation (3) amounted to 0.7.

$$X_A = \frac{0.79 \cdot I_A}{0.79 \cdot I_A + I_R'} \quad (3)$$

where I_A and I_R are the integrated intensities of the most intense peaks of anatase (011) and rutile (110) phases, respectively. The diffraction peaks observed at $2\theta = 30.1^\circ$ (171), 33.1° (200) and 42.8° (113) indexed to orthorhombic Bi₄Ti₃O₁₂ with Aba2 space group (ICSD reference code: 98-008-7809) [28]. The peaks can be indexed to a pure hexagonal structure with R3c space group for BiFeO₃ observed at around $2\theta = 31.7^\circ$ (104) and 32.1° (110) (ICSD Reference code: 98-001-5299) [29] and shown in the right insert in Figure 4. The other peaks correspond to orthorhombic Bi₆Fe₂Ti₃O₁₈ with Fmm2 space group. Deconvolution of the peaks in the left insert in Figure 4 indicates the phase of Bi₄Ti₃O₁₂ at 29.9° (171) and of Bi₆Fe₂Ti₃O₁₈ at 30.4° (11 11). Presence of Bi₄Ti₃O₁₂ and BiFeO₃ phases confirms the suggested method of structure formation of Aurivillius phase.

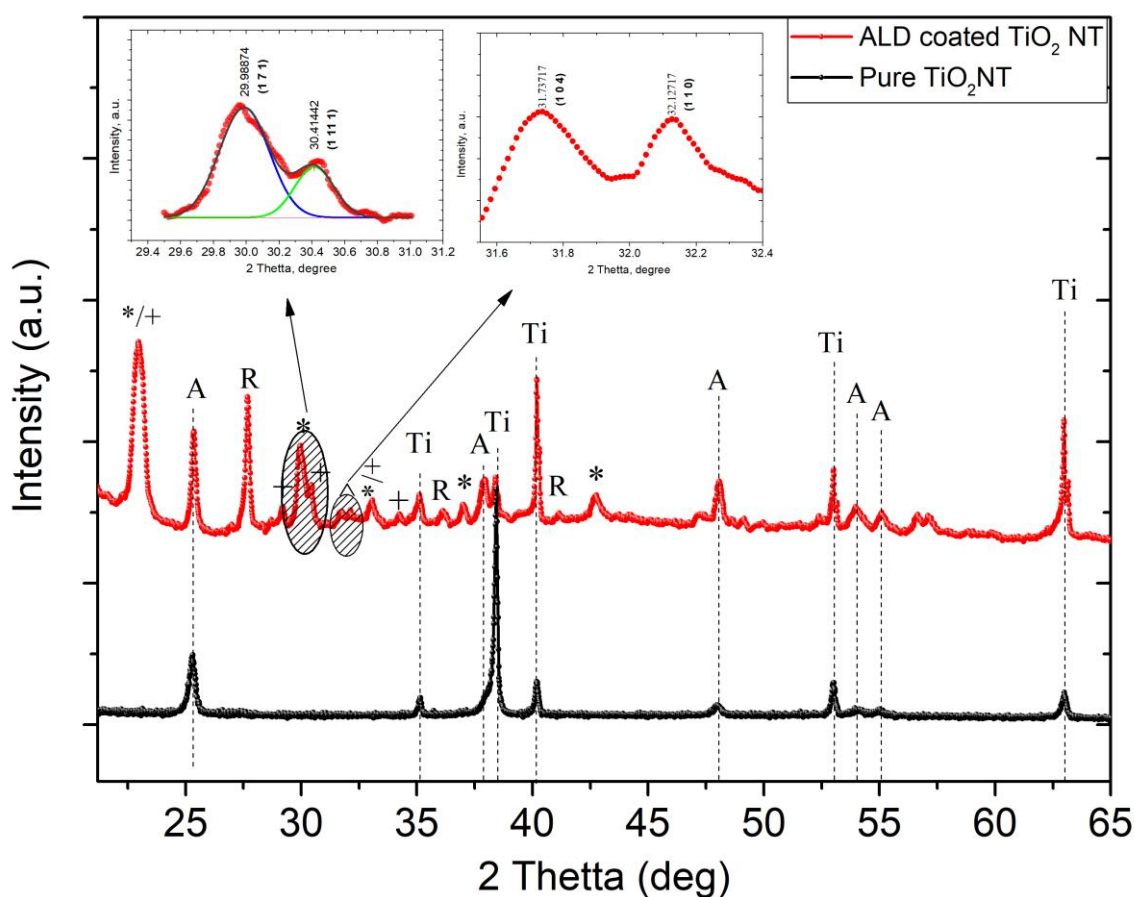


Figure 4. XRD patterns of pure and ALD-coated TiO_2 Nt. A—anatase; Ti—titanium; R—rutile; *— $\text{Bi}_4\text{Ti}_3\text{O}_{12}$; +— $\text{Bi}_6\text{Fe}_2\text{Ti}_3\text{O}_{18}$; ^— BiFeO_3 . Insert (left)—deconvoluted $\text{Bi}_4\text{Ti}_3\text{O}_{12}/\text{Bi}_6\text{Fe}_2\text{Ti}_3\text{O}_{18}$ peaks, (right)— BiFeO_3 peaks.

Since Raman spectroscopy is sensitive to atomic displacements, it can provide valuable information on lattice properties and structural transitions. Raman spectra were obtained and the data are presented in Figure 5a. For comparison, the spectra of the pure TiO_2 Nt crystallized in the anatase phase are also presented. The low-frequency region of the Raman spectra of layered bismuth compounds (below 200 cm^{-1}) refers to vibrations of Bi^{3+} ions in the $(\text{Bi}_2\text{O}_2)^{2+}$ layer and vibrations of Bi^{3+} ions relative to oxygen octahedra. The high-frequency modes above 200 cm^{-1} characterize the bending and tensile modes of the BO_6 octahedron [30]. The characteristic TiO_2 modes of anatase and rutile phases are observed in the spectra [31]. Rutile appears because of anatase–rutile transformation that occurs at $660\text{ }^\circ\text{C}$ during annealing. It should be noted that almost all high-frequency modes are asymmetric; therefore, they can be interpreted as a superposition of several closely located Raman modes. The peak at 340 cm^{-1} corresponds to the torsional bending of the octahedra Ti/FeO_6 . Modes at 567 and 800 cm^{-1} are connected with stretching octahedral O–Ti/Fe chains between $(\text{Bi}_2\text{O}_2)^{2+}$ layers. The asymmetric peak in the 844 cm^{-1} region corresponds to fully symmetric stretching vibrations of the O–Ti–O and O–Fe–O bonds in the Ti/FeO_6 octahedra. The appearance of phonon modes at 567 and 706 cm^{-1} occurs due to a combination of the stretching of the Bi–Fe–O bond and the octahedral bending [32,33]. The Raman modes at about 222 , 267 and 535 cm^{-1} , are attributed to the internal vibrational modes of Ti/FeO_6 octahedrons in BFTO [32]. In addition, the characteristic peaks of BiFeO_3 (green arrows) and $\text{Bi}_4\text{Ti}_3\text{O}_{12}$ (blue arrows) are observed in the spectrum [34,35].

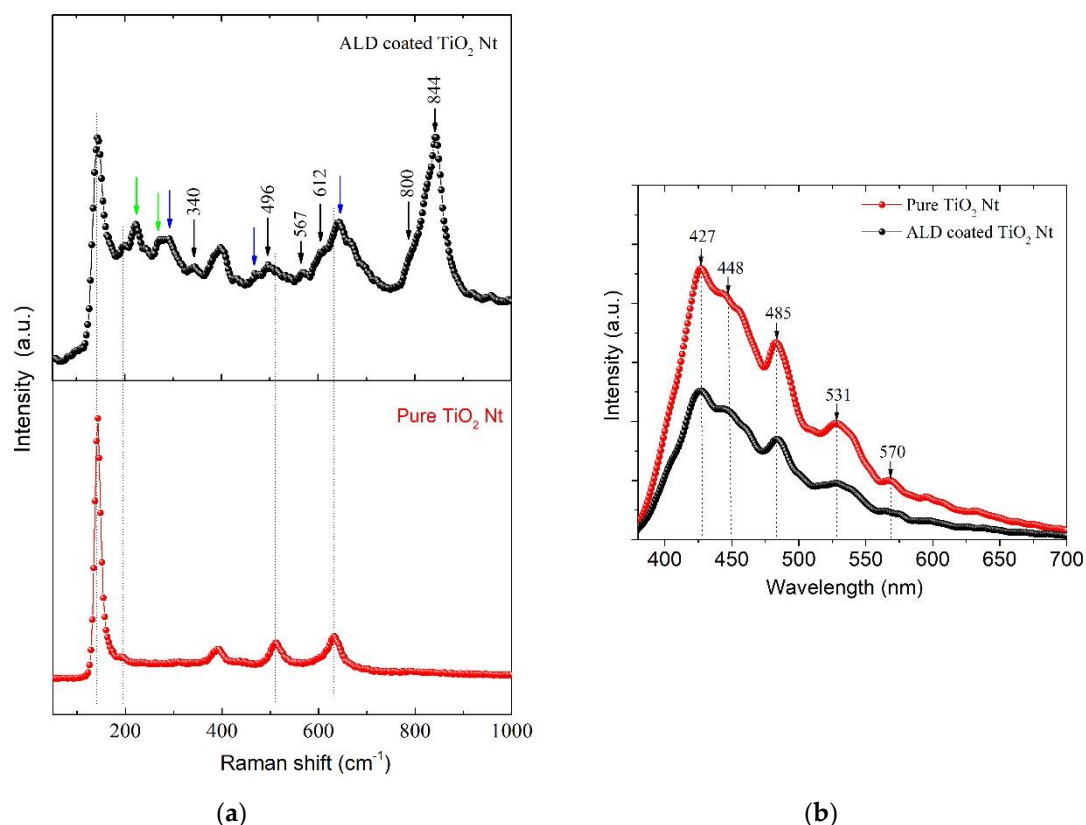


Figure 5. (a) Raman and (b) photoluminescence spectra for pure and ALD-coated TiO₂ Nt.

Photoluminescence (PL) analysis is commonly used to analyze the recombination rate of photo-generated electron-hole of TiO₂. Herein, we conduct PL measurement for pure and ALD-coated TiO₂ Nt samples (Figure 5b). PL radiation intensity refers to the recombination of excited electrons and holes. Lowering the PL intensity indicates a decrease in the probability of recombination. It can be seen that the emission spectra are similar. When compared with pure TiO₂, the intensity of the PL signal for ALD-coated TiO₂ Nt is much lower.

This is due to the reduction in the radiative recombination process—that is, the lower the recombination, the weaker the PL signals are [36,37]. The spectra show broad emission in the visible range (350–600 nm). Two PL peaks at 427 and 448 nm correspond to self-trapped excitons (STE) localized on TiO₆ octahedra and oxygen vacancies with two electrons, respectively (F centers) [38]. The broad peak at 531 nm is caused by an oxygen vacancy with one captured electron (F⁺ center) [39]. The peaks at 485 and 570 nm correspond to oxygen vacancies with one electron and surface oxygen vacancies (Vo). The presence of oxygen vacancies contributes to a more efficient photocatalytic process. The effective charge carrier separation extends the reactive electron and hole lifetimes [40] and enhances the photocatalytic activity of the photocatalysts.

To determine the valence state of ions for ALD-coated TiO₂ NT, room temperature X-ray photoelectron spectroscopy studies were performed. Figure 6a shows the X-ray photoelectron spectroscopy survey spectra from 0 to 750 eV. The core level energies associated with Fe, Bi, Ti, O and C elements are identified. Five regions related with Fe 2p, Bi 4f, Ti 2p and O 1s of the survey XPS spectra for compounds were analyzed. High resolution spectra of Bi4f core level are shown in Figure 6a. Peaks Bi 4f_{7/2} and Bi 4f_{5/2} at ~159.0 eV and ~164.3 eV, respectively, correspond to Bi₂O₃. The energy of the spin-orbit splitting of the Bi 4f doublet is equal to 5.3 eV (the energy difference between Bi 4f_{7/2} and Bi 4f_{5/2}) and consistent with previously reported experimental and theoretical values. Probably, the asymmetry of the Bi 4f_{7/2} and Bi 4f_{5/2} peaks indicates the presence of bismuth ions with other oxidation states that differ from +3 [41].

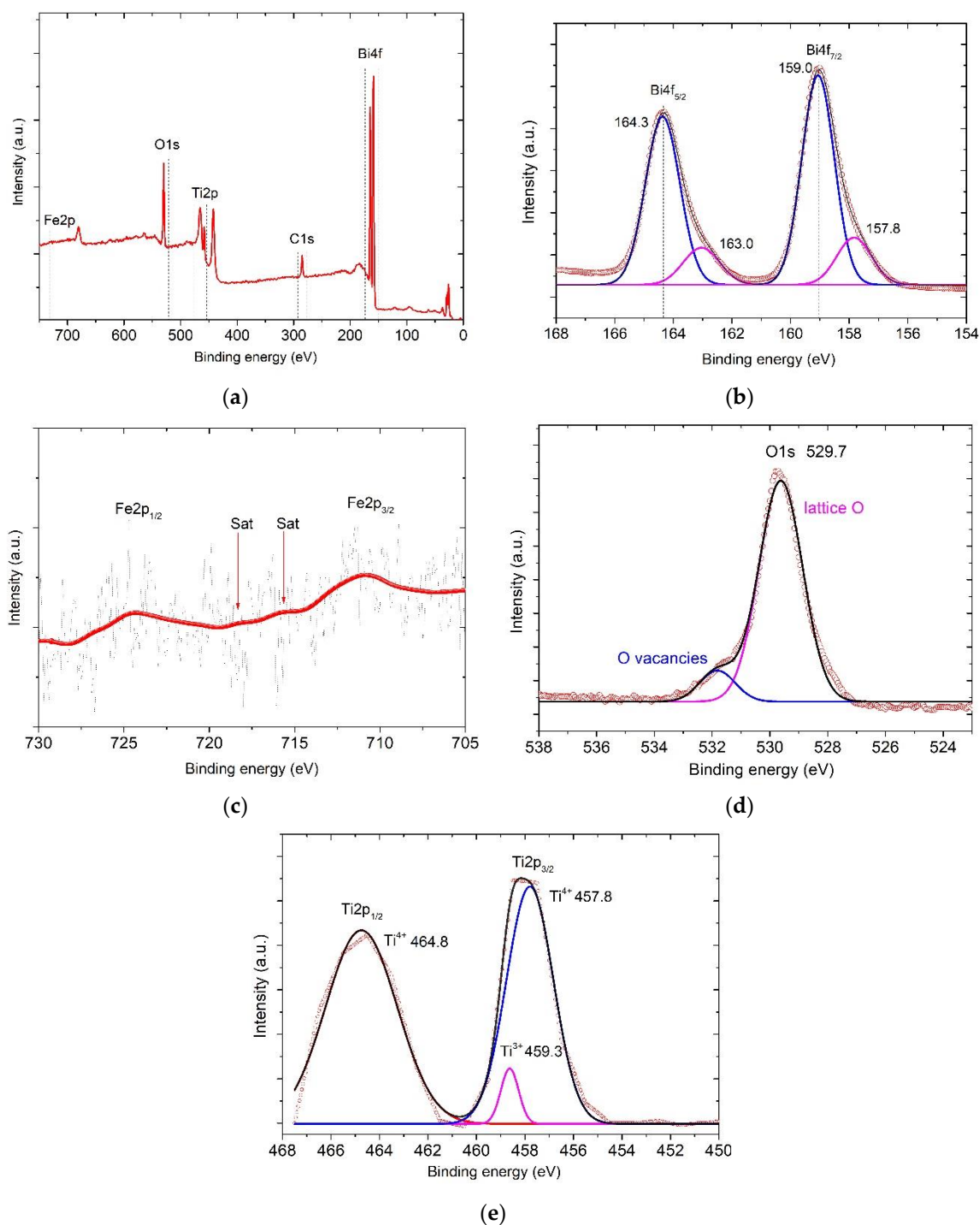
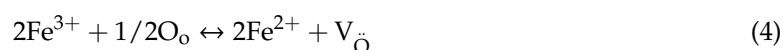


Figure 6. (a) Survey X-ray photoelectron spectrometer (XPS) spectra for the ALD-coated TiO₂ NT. (b) High-resolution Bi 4f spectra; (c) high-resolution Fe 2p spectra; (d) high-resolution O 1s spectra; (e) high-resolution Ti 2p spectra.

The spectra of Fe 2p core level are shown in Figure 6c. The signal is weak and a similar situation was observed in other works [42,43] but the reason is still unknown. The peaks' asymmetry indicates the presence of mixed valence of iron cations [44].

Oxygen vacancies will occur in the presence of Fe²⁺ ions in the structure [45], which are necessary to maintain electroneutrality of the system, according to the Kröger–Vink notation:



Oxygen vacancies reduce intrinsic defects on particle surfaces, which are a well-known capture center for carrier recombination. This effect promotes electron–hole separation in lattices and causes increasing photocatalytic efficiency [46].

The core-level spectra of Ti 2p are shown in Figure 6e. The spin-orbit splitting of Ti 2p_{1/2} and Ti 2p_{3/2} peaks located at around 464.7 and 457.8 eV, respectively, corresponds to the binding energy of Ti 2p_{1/2} and Ti 2p_{3/2}. These peaks are consistent with Ti⁴⁺ in TiO₂ lattice [47]. Furthermore, the shoulder Ti 2p_{1/2} at binding energy 459.3 eV corresponds to Ti³⁺ in Ti₂O₃ [48]. The appearance of Ti³⁺ is caused by the partial replacing of titanium atoms by iron atoms in TiO₆ octahedra. A similar effect was observed at doping of TiO₂ films with iron ions [49]. In this case, at Ti⁴⁺/Ti³⁺ transition, oxygen vacancies will be formed in the structure for charge balance, similar to Fe³⁺/Fe²⁺ transition, as was mentioned above. It could be confirmed by high resolution XPS spectra of the O 1s peak (Figure 6d). The intensive peak at 529.7 eV belongs to lattice oxygen. The shoulder at 531.5 eV corresponds to defect oxygen components as oxygen vacancy.

The optical properties of the samples were studied by UV-Vis diffuse reflection. Figure 7a shows the diffuse reflectance spectra presented in the Kubelka–Munk absorption coordinates. The appearance of the shoulder in the visible region and the shift of the absorption edge of the heterostructure towards large wavelengths could be observed. The absorption at the 330 nm wavelength is connected with the indirect transition of phonons from the edges to the center of the Brillouin zone [50]. It was shown by Sun et al. [9], by ab initio calculations, that the valence band in layered perovskites mainly consists of hybrid orbits O 2p + Fe t_{2g} + Bi 6s and the conduction band consists mainly of orbits Ti 3d + Fe e_g. In this case, the electronic excitation from hybridized orbits O 2p + Fe t_{2g} + Bi 6s to Fe e_g orbits should be responsible for the absorption of photons of visible light, and the electronic excitation from hybrid orbits O 2p + Fe t_{2g} + Bi 6s to 3d orbits of Ti corresponds to the absorption of photons of ultraviolet light. It can be concluded that using UV-Vis radiation will be more effective for photocatalysis of ALD-coated TiO₂ Nt. Figure 7b shows the energy (hν) dependence of the direct allowed inter-band transition (αhν)². The band gap of the films was estimated by the traditional Tauc's relation:

$$\alpha h\nu = A(h\nu - E_g)^n \quad (5)$$

where A—constant; hν—photon energy; α—absorption coefficient; E_g—energy of the optical band gap; n— $\frac{1}{2}$ in the case of indirect and 2 in the case of direct inter-band transition. The direct and indirect band gaps for pure TiO₂ Nt are 2.84 and 3.05 eV, for ALD-coated TiO₂ Nt are 2.67 and 2.31 eV, respectively. As expected, the (E_g) of the ALD-coated TiO₂ Nt decreases due to the fact that the E_g of pure TiO₂ Nt is higher than in compounds of the Aurivillius phases [9,51]. Here, the decrease in the value of the band gap is apparently explained by the presence of additional energy states near the edge of the conduction band, which is caused by the disorder of the crystal lattice formed during the deposition of the coating. It is known that the distribution of the density of electronic states determines the physical characteristics of a material and the processes occurring in it: optical absorption, conductivity and photoconductivity. The density of localized electronic states in synthesized systems can be evaluated from the Urbach characteristic energy, which can be calculated from the rate of exponential decay of the “tail” in the absorption spectrum. The width of the Urbach tail is an indicator of the disorder in the material. Urbach energy tail is evaluated according to the Urbach law [52].

$$\alpha = \alpha_0 \exp\left(\frac{h\nu}{E_U}\right) \quad (6)$$

$$E_U = \left[\frac{d \ln \alpha}{d h\nu}\right]^{-1} \quad (7)$$

where α₀—constant; E_U—Urbach energy, which characterizes the slope of the exponential limit. The E_U is calculated from the inverse dependence of the slope ln α on hν in the region slightly below the band gap [53]. Results are presented in Figure 7c,d. The calculated values of Urbach energy are 96 meV

for pure TiO₂ Nt and 409 meV for ALD-coated TiO₂ Nt. A significant increase in the E_U for ALD-coated TiO₂ Nt indicates the appearance of impurity energy levels in the band gap. These energy levels can be associated with the coexistence of one-dimensional (1D) phase-modulated structures consisting of two different layered Aurivillius phases with alternating the number of five and six perovskite-like layers with different Fe/Ti ratio in the octahedra and structural disorder due to the presence of oxygen and bismuth vacancies [54]. This is consistent with the conclusion of B. Choudhury and A. Choudhury [55] where they mention that the energy increase is caused by the presence of oxygen vacancies and structural disorder at the interface of different phases. It confirms that the PL and UV-Vis spectroscopy data are in good agreement and indicate the prospect of using the obtained materials as photocatalysts, since the oxygen vacancies play an essential role in photocatalytic reactions [56].

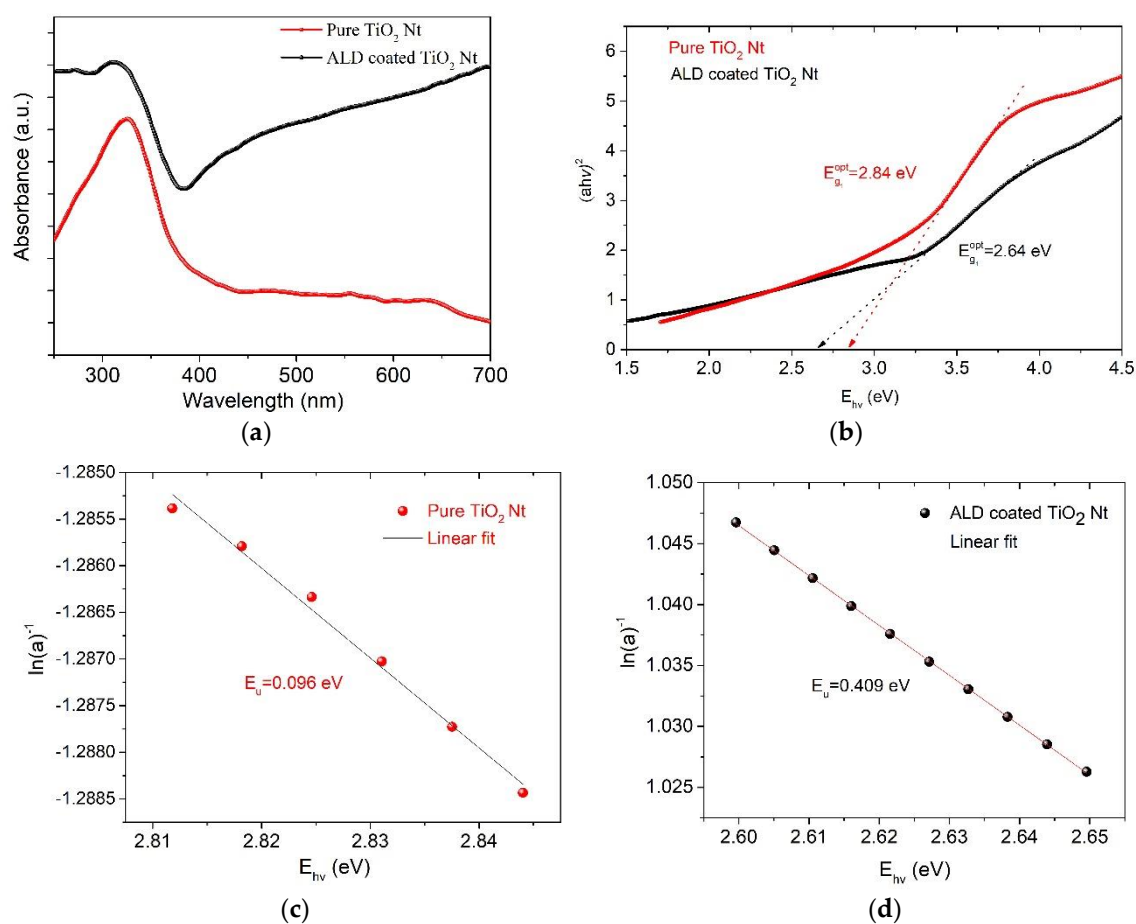


Figure 7. Optical properties of pure and ALD-coated TiO₂ Nt. (a) UV-Vis spectra, (b) Tauc plots for indirect transition and (c) determination of Urbach energy for pure and (d) ALD-coated TiO₂ Nt.

The degradation of MO solution with 5 mg/L concentration was utilized as a probe to investigate the photoelectrocatalytic activities of both pure and ALD-coated TiO₂ Nt for comparison. Figure 8a shows the region of the absorption spectrum of the MO solution around the wavelength of 466 nm. This sector is characterized by the presence of -N=N- bonds, of which the dynamics reflect the discoloration process. The red line (Figure 8b) shows the residual MO concentration after 60 min of the PEC process using pure TiO₂ Nt as the photoelectrode. The black lines (Figure 8a) show the kinetics of the PEC process using ALD-coated TiO₂ Nt as the photoelectrode. It can be seen that the sample of ALD-coated TiO₂ Nt showed the best PEC activity. Almost 100% of MO removal was observed in 60 min of the process, while for pure TiO₂ Nt, it was 72%. PEC degradation of MO with both photoelectrodes obeys the first-order reaction kinetics as shown in Figure 8b. The decomposition rate of MO using ALD-coated TiO₂ Nt increases more than two times according to the calculated values of the rate constants. A

cycling test was carried out since the stability of the photoelectrodes is very important. Figure 8c presents the long-term stability of ALD-coated TiO₂ Nt in the PEC MO degradation process. As can be seen after five cycles, the PEC degradation ratio is maintained at 95%, suggesting good stability.

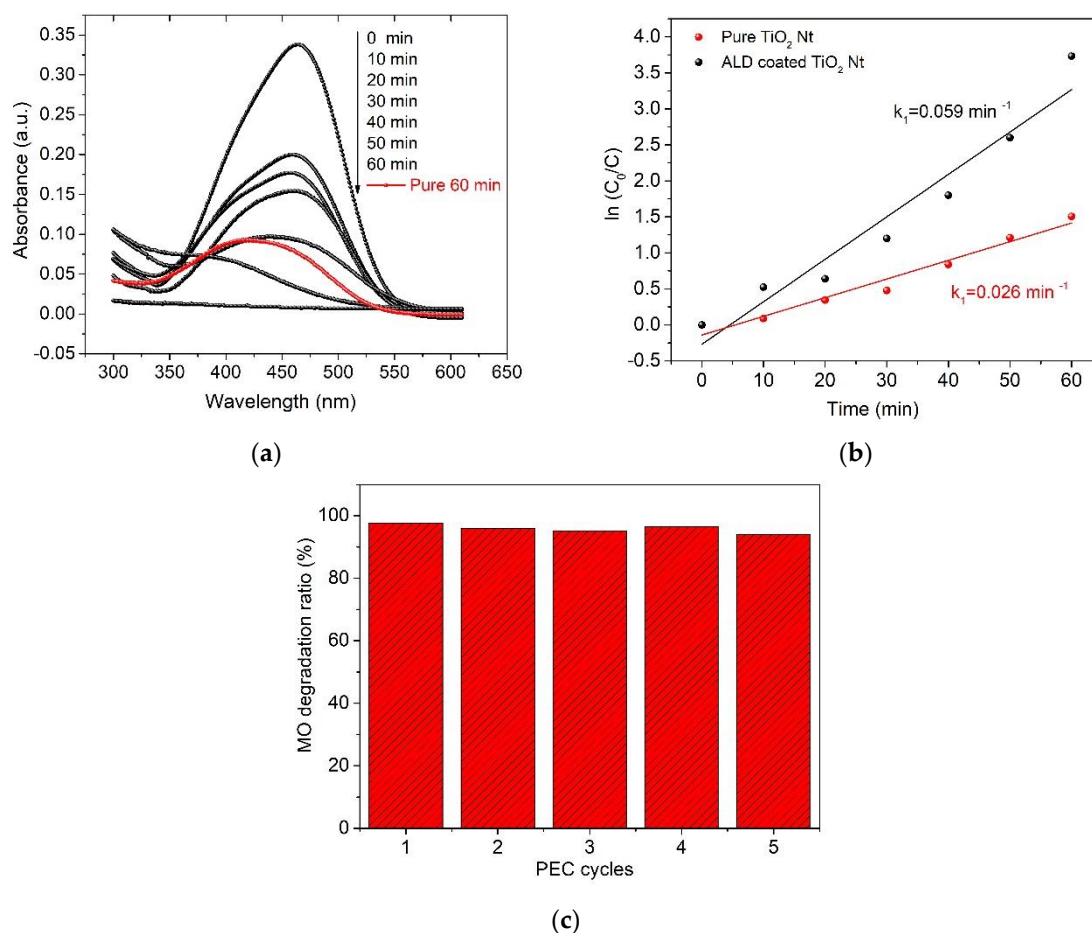


Figure 8. Temporal absorption spectral patterns of methyl orange (MO) during the photoelectrocatalytic process (a) using pure and ALD-coated TiO₂ Nt under UV-Vis light irradiation. (b) First-order reaction kinetics curves. (c) Photoelectrocatalysis cycles of MO degradation using ALD-coated TiO₂ Nt under UV-Vis light irradiation.

The enhancement of the photon excitation efficiency of electrons due to the ALD coating is confirmed by the observation of the difference in photocurrent between pure and ALD-coated TiO₂ Nt. The photocurrent was measured under pulsed irradiation of UV-Vis light. The induced photocurrents of the samples are well correlated with pulsed irradiation of UV-Vis light (Figure 9). The ALD-coated TiO₂ Nt have a stronger photoresponse than the pure TiO₂ Nt. The photocurrent peak of ALD-coated TiO₂ Nt is about 23% higher than for pure nanotubes because of easier photoinduced electronic excitation. Both photoelectrodes showed relatively good reproducibility and stability when lights were turned on and off. Both samples showed the anode photocurrent when the light was turned on, which is typical for n-type semiconductors. However, when the illumination is turned off, a dark negative current is detected in the cell with the ALD-coated TiO₂ Nt and this value slowly reached saturation and stabilized. A similar effect was observed by B. Ouyang et al. [57], where the authors described the SnS/ZnO system with a p-n heterojunction and explained the appearance of a negative current after the lighting is turned off by the complex effect of photoexcitation arising from photoabsorption and thermo-potential inside SnS. In view of the presence of various properties (piezoelectric effect) in layered compounds of the Aurivillius phases, which can be responsible for this effect, the explanation in our case is still not clear. Further studies are needed in order to understand the observed phenomenon.

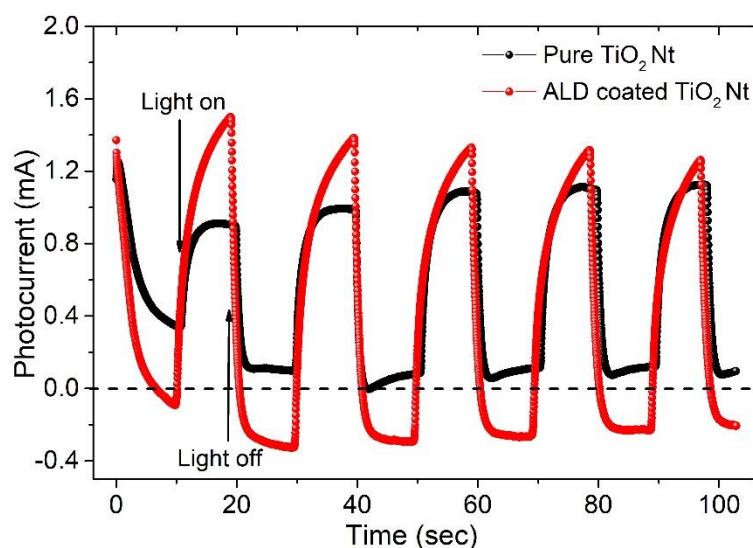


Figure 9. Transient photocurrent responses under Ultraviolet–Visible (UV-Vis) light irradiation.

This result can be explained considering that TiO_2 is an n-type semiconductor [58] and layered perovskites of the Aurivillius phase exhibit ionic-p-type electronic mixed conduction [59]. The p-type electrical conductivity is due to oxygen vacancies in the bismuth oxide layer. Thus, a p-n heterojunction is formed at the BFTO-TiO_2 Nt interface, in which an internal electric field is present because of the spatial separation of charges. According to literature [8], the edge of the n-type TiO_2 conduction band (CB) is located above the CB of the BFTO edge, which makes the transitions of the photogenerated electrons from BFTO to TiO_2 thermodynamically unfavorable; however, holes can easily transfer from n-type TiO_2 to p-type BFTO [60]. This limits the recombination and contributes to a more efficient separation of photogenerated electron–hole pairs.

4. Conclusions

One-dimensional phase-modulated structures of layered Aurivillius phases with alternating 5 and 6-layer perovskite-like blocks were obtained on the surface of TiO_2 Nt by ALD using the methodology of a two-layer $\text{Bi}_2\text{O}_3\text{-FeO}_x$ sandwich structure. It is shown that the layered structure is formed due to self-organization during annealing at 660°C . The results of PL spectroscopy indicate a high application potential in photocatalysis and photoelectrochemistry due to a decrease in the radiative recombination of charges. Diffuse reflection spectroscopy demonstrated a narrowing of the band gap due to defective energy states associated with disorder of the crystal lattice. The 4.2-times increase in the Urbach energy for ALD-coated TiO_2 Nt characterizes the structural disorder associated with the presence of oxygen and bismuth vacancies and coexistence of 1D phase-modulated structures consisting of two different layered Aurivillius phases with alternating the number of five and six perovskite-like layers with different Fe/Ti ratio in the octahedra. Transient photocurrent responses under UV-Vis light irradiation show that the ALD coating benefits the efficiency of photon excitation of electrons. The results of the PEC experiments and MO photodegradation demonstrate the significant potential of the synthesized structure as a photocatalyst.

Supplementary Materials: The following are available online at <http://www.mdpi.com/2079-4991/10/11/2183/s1>, Figure S1: Emission spectrum of 250 W discharge mercury vapor lamp with a preliminary removed phosphor layer.

Author Contributions: Conceptualization, F.O.; methodology, F.O., S.R., A.M. and M.K.; software, F.O. and S.R.; validation, F.O., A.I. and C.W.; formal analysis, D.S.; investigation, D.S., A.M. and M.K.; resources, A.I.; data curation, A.I., K.K. and C.W.; writing—original draft preparation, F.O. and D.S.; writing—review and editing, K.K.; visualization, F.O. and K.K.; supervision, F.O.; funding acquisition, A.I. and D.S. All authors have read and agreed to the published version of the manuscript.

Funding: The reported study was funded by RFBR according to the research project № 20-33-90220. The research was supported by the Ministry of Education, Youth and Sports of the Czech Republic under the project CEITEC 2020 (grant number LQ1601, 2020). A part of the work was carried out with the support of CEITEC Nano Research Infrastructure (grant number LM2015041, MEYS CR, 2016–2019), CEITEC Brno University of Technology.

Conflicts of Interest: The authors declare no conflict of interest and no known competing financial interests or personal relationships that could have appeared to influence the work reported in this paper.

References

1. Krzhizhanovskaya, M.; Filatov, S.; Gusarov, V.; Paufler, P.; Bubnova, R.; Morozov, M.; Meyer, D.C. Aurivillius phases in the $\text{Bi}_4\text{Ti}_3\text{O}_{12}/\text{BiFeO}_3$ system: Thermal behaviour and crystal structure. *Z. Anorg. Allg. Chem.* **2005**, *631*, 1603–1608. [[CrossRef](#)]
2. Lomanova, N.A.; Morozov, M.I.; Ugolkov, V.L.; Gusarov, V.V. Properties of Aurivillius phases in the $\text{Bi}_4\text{Ti}_3\text{O}_{12}\text{-BiFeO}_3$ system. *Inorg. Mater.* **2006**, *42*, 189–195. [[CrossRef](#)]
3. Lomanova, N.A.; Semenov, V.G.; Panchuk, V.V.; Gusarov, V.V. Structural changes in the homologous series of the Aurivillius phases $\text{Bi}_{n+1}\text{Fe}_{n-3}\text{Ti}_3\text{O}_{3n+3}$. *J. Alloys Compd.* **2012**, *528*, 103–108. [[CrossRef](#)]
4. Deepak, N.; Carolan, P.; Keeney, L.; Pemble, M.E.; Whatmore, R.W. Tunable nanoscale structural disorder in Aurivillius phase, $n = 3$ $\text{Bi}_4\text{Ti}_3\text{O}_{12}$ thin films and their role in the transformation to $n = 4$, $\text{Bi}_5\text{Ti}_3\text{FeO}_{15}$ phase. *J. Mater. Chem. C* **2015**, *3*, 5727–5732. [[CrossRef](#)]
5. García-Guaderrama, M.; Fuentes, L.; Márquez-Lucero, A.; Blanco, O. Structural stability and cation disorder in Aurivillius phases. *Mater. Res. Bull.* **2012**, *47*, 3850–3854. [[CrossRef](#)]
6. Wu, M.; Tian, Z.; Yuan, S.; Huang, Z. Magnetic and optical properties of the Aurivillius phase $\text{Bi}_5\text{Ti}_3\text{FeO}_{15}$. *Mater. Lett.* **2012**, *68*, 190–192. [[CrossRef](#)]
7. Yan, S.; Feng, Z.; Ma, Z.; Zhang, Y.; Ye, W. Multiferroic properties of $\text{Bi}_5\text{Ti}_3\text{FeO}_{15}$ ceramics prepared by hot-pressing methods. *Mater. Lett.* **2018**, *227*, 247–249. [[CrossRef](#)]
8. Ola, O.; Maroto-Valer, M.M. Review of material design and reactor engineering on TiO_2 photocatalysis for CO_2 reduction. *J. Photochem. Photobiol. C Photochem. Rev.* **2015**, *24*, 16–42. [[CrossRef](#)]
9. Sun, S.; Wang, W.; Xu, H.; Zhou, L.; Shang, M.; Zhang, L. $\text{Bi}_5\text{FeTi}_3\text{O}_{15}$ hierarchical microflowers: Hydrothermal synthesis, growth mechanism, and associated visible-light-driven photocatalysis. *J. Phys. Chem. C* **2008**, *112*, 17835–17843. [[CrossRef](#)]
10. Naresh, G.; Malik, J.; Meena, V.; Mandal, T.K. PH-Mediated Collective and Selective Solar Photocatalysis by a Series of Layered Aurivillius Perovskites. *ACS Omega* **2018**, *3*, 11104–11116. [[CrossRef](#)]
11. Abbas, W.A.; Abdullah, I.H.; Ali, B.A.; Ahmed, N.; Mohamed, A.M.; Rezk, M.Y.; Ismail, N.; Mohamed, M.A.; Allam, N.K. Recent advances in the use of TiO_2 nanotube powder in biological, environmental, and energy applications. *Nanoscale Adv.* **2019**, *1*, 2801–2816. [[CrossRef](#)]
12. Dvorak, F.; Zazpe, R.; Krbal, M.; Sopha, H.; Prikryl, J.; Ng, S.; Hromadko, L.; Bures, F.; Macak, J.M. One-dimensional anodic TiO_2 nanotubes coated by atomic layer deposition: Towards advanced applications. *Appl. Mater. Today* **2019**, *14*, 1–20. [[CrossRef](#)]
13. Orudzhev, F.F.; Aliev, Z.M.; Gasanova, F.G.; Isaev, A.B.; Shabanov, N.S. Photoelectrocatalytic Oxidation of Phenol on TiO_2 Nanotubes under Oxygen Pressure. *Russ. J. Electrochem.* **2015**, *51*, 1247–1253. [[CrossRef](#)]
14. Sobola, D.; Ramazanov, S.; Konečný, M.; Orudzhev, F.; Kaspar, P.; Papež, N.; Knápek, A.; Potoček, M. Complementary SEM-AFM of Swelling Bi-Fe-O Film on HOPG Substrate. *Materials* **2020**, *13*, 2402. [[CrossRef](#)] [[PubMed](#)]
15. Ramazanov, S.; Sobola, D.; Orudzhev, F.; Knápek, A.; Polčák, J.; Potoček, M.; Dallaev, R. Surface Modification and Enhancement of Ferromagnetism in BiFeO_3 Nanofilms Deposited on HOPG. *Nanomaterials* **2020**, *10*, 1990. [[CrossRef](#)] [[PubMed](#)]
16. Leu, C.C.; Lin, T.J.; Chen, S.Y.; Hu, C.T. Effects of bismuth oxide buffer layer on BiFeO_3 thin film. *J. Am. Ceram. Soc.* **2015**, *98*, 724–731. [[CrossRef](#)]
17. Akbashev, A.R.; Chen, G.; Spanier, J.E. A facile route for producing single-crystalline epitaxial perovskite oxide thin films. *Nano Lett.* **2014**, *14*, 44–49. [[CrossRef](#)] [[PubMed](#)]
18. Shen, Y.D.; Li, Y.W.; Li, W.M.; Zhang, J.Z.; Hu, Z.G.; Chu, J.H. Growth of Bi_2O_3 ultrathin films by atomic layer deposition. *J. Phys. Chem. C* **2012**, *116*, 3449–3456. [[CrossRef](#)]
19. Aurivillius, B. Mixed Bismuth Oxides with Layer lattices: I. The Structure Type of $\text{CaBi}_2\text{Nb}_2\text{O}_9$. *Ark. Kemi Band I* **1949**, *54*, 463–480.

20. Lu, C.D.; Chang, L.S.; Lu, Y.F.; Lu, F.H. The growth of interfacial compounds between titanium dioxide and bismuth oxide. *Ceram. Int.* **2009**, *35*, 2699–2704. [[CrossRef](#)]
21. Morozov, M.I.; Gusarov, V.V. Synthesis of $A_{m-1}Bi_2M_mO_{3m+3}$ compounds in the $Bi_4Ti_3O_{12}$ - $BiFeO_3$ system. *Inorg. Mater.* **2002**, *38*, 723–729. [[CrossRef](#)]
22. Sun, S.; Wang, G.; Huang, Y.; Wang, J.; Peng, R.; Lu, Y. Structural transformation and multiferroic properties in Gd-doped $Bi_7Fe_3Ti_3O_{21}$ ceramics. *RSC Adv.* **2014**, *4*, 30440–30446. [[CrossRef](#)]
23. Sun, S.; Chen, Z.; Wang, G.; Geng, X.; Xiao, Z.; Sun, Z.; Sun, Z.; Peng, R.; Lu, Y. Nanoscale Structural Modulation and Lower-temperature Magnetic Response in Mixed-layer Aurivillius-type Oxides. *Sci. Rep.* **2018**, *8*, 871. [[CrossRef](#)] [[PubMed](#)]
24. Sun, S.; Yan, H.; Wang, G.; Wang, J.; Peng, R.; Fu, Z.; Zhai, X.; Mao, X.; Chen, X.; Lu, Y. Room-temperature multiferroic responses arising from 1D phase modulation in correlated Aurivillius-type layer structures. *J. Phys. D Appl. Phys.* **2016**, *49*, 125005. [[CrossRef](#)]
25. Armstrong, R.A.; Newnham, R.E. Bismuth titanate solid solutions. *Mater. Res. Bull.* **1972**, *7*, 1025–1034. [[CrossRef](#)]
26. Kikuchi, T. Stability of layered bismuth compounds in relation to the structural mismatch. *Mater. Res. Bull.* **1979**, *14*, 1561–1569. [[CrossRef](#)]
27. Macak, J.M.; Tsuchiya, H.; Ghicov, A.; Yasuda, K.; Hahn, R.; Bauer, S.; Schmuki, P. TiO_2 nanotubes: Self-organized electrochemical formation, properties and applications. *Curr. Opin. Solid State Mater. Sci.* **2007**, *11*, 3–18. [[CrossRef](#)]
28. Achary, S.N.; Patwe, S.J.; Krishna, P.S.R.; Shinde, A.B.; Tyagi, A.K. Cation disorder and structural studies on $Bi_{4-x}Nd_xTi_3O_{12}$ ($0.0 \leq x \leq 2.0$). *Pramana J. Phys.* **2008**, *71*, 935–940. [[CrossRef](#)]
29. Zhang, S.T.; Lu, M.H.; Wu, D.; Chen, Y.F.; Ming, N.B. Larger polarization and weak ferromagnetism in quenched $BiFeO_3$ ceramics with a distorted rhombohedral crystal structure. *Appl. Phys. Lett.* **2005**, *87*, 262907. [[CrossRef](#)]
30. Venkata Ramana, E.; Prasad, N.V.; Figueiras, F.; Lajaunie, L.; Arenal, R.; Otero-Irurueta, G.; Valente, M.A. The growth and improved magnetoelectric response of strain-modified Aurivillius $SrBi_{4.25}La_{0.75}Ti_4FeO_{18}$ thin films. *Dalt. Trans.* **2019**, *48*, 13224–13241. [[CrossRef](#)]
31. Giorgi, L.; Dikonimos, T.; Giorgi, R.; Buonocore, F.; Faggio, G.; Messina, G.; Lisi, N. Electrochemical synthesis of self-organized TiO_2 crystalline nanotubes without annealing. *Nanotechnology* **2018**, *29*, 095604. [[CrossRef](#)]
32. Du, Y.L.; Chen, G.; Zhang, M.S. Grain size effects in $Bi_4Ti_3O_{12}$ nanocrystals investigated by Raman spectroscopy. *Solid State Commun.* **2004**, *132*, 175–179. [[CrossRef](#)]
33. Rodríguez Aranda, M.D.C.; Rodríguez-Vázquez, Á.G.; Salazar-Kuri, U.; Mendoza, M.E.; Navarro-Contreras, H.R. Raman effect in multiferroic $Bi_5Fe_{1+x}Ti_{3-x}O_{15}$ solid solutions: A temperature study. *J. Appl. Phys.* **2018**, *123*, 084101. [[CrossRef](#)]
34. Rodrigues, H.O.; Pires Junior, G.F.M.; Sales, A.J.M.; Silva, P.M.O.; Costa, B.F.O.; Alcantara, P.; Moreira, S.G.C.; Sombra, A.S.B. $BiFeO_3$ ceramic matrix with Bi_2O_3 or PbO added: Mössbauer, Raman and dielectric spectroscopy studies. *Phys. B Condens. Matter* **2011**, *406*, 2532–2539. [[CrossRef](#)]
35. Quintana-Celleruelo, J.Á.; Veerapandiyam, V.K.; Deluca, M.; Algueró, M.; Castro, A. Mechano-synthesis of the whole $Y_{1-x}Bi_xMn_{1-x}Fe_xO_3$ perovskite system: Structural characterization and study of phase transitions. *Materials* **2019**, *12*, 1515. [[CrossRef](#)] [[PubMed](#)]
36. Lv, K.; Hu, J.; Li, X.; Li, M. Cysteine modified anatase TiO_2 hollow microspheres with enhanced visible-light-driven photocatalytic activity. *J. Mol. Catal. A Chem.* **2012**, *356*, 78–84. [[CrossRef](#)]
37. Yu, J.; Ma, T.; Liu, S. Enhanced photocatalytic activity of mesoporous TiO_2 aggregates by embedding carbon nanotubes as electron-transfer channel. *Phys. Chem. Chem. Phys.* **2011**, *13*, 3491–3501. [[CrossRef](#)]
38. Iatsunskyi, I.; Coy, E.; Viter, R.; Nowaczyk, G.; Jancelewicz, M.; Baleviciute, I.; Załeski, K.; Jurga, S. Study on Structural, Mechanical, and Optical Properties of Al_2O_3 - TiO_2 Nanolaminates Prepared by Atomic Layer Deposition. *J. Phys. Chem. C* **2015**, *119*, 20591–20599. [[CrossRef](#)]
39. Li, D.; Haneda, H.; Hishita, S.; Ohashi, N. Visible-light-driven N-F-codoped TiO_2 photocatalysts. 2. Optical characterization, photocatalysis, and potential application to air purification. *Chem. Mater.* **2005**, *17*, 2596–2602. [[CrossRef](#)]
40. Zhu, A.; Zhao, Q.; Li, X.; Shi, Y. $BiFeO_3/TiO_2$ Nanotube Arrays Composite Electrode: Construction, Characterization, and Enhanced Photoelectrochemical Properties. *ACS Appl. Mater. Interfaces* **2014**, *6*, 671–679. [[CrossRef](#)] [[PubMed](#)]

41. Zhang, G.; Cai, L.; Zhang, Y.; Wei, Y. Bi^{5+} , $\text{Bi}^{(3-x)+}$, and Oxygen Vacancy Induced $\text{BiOCl}_x\text{I}_{1-x}$ Solid Solution toward Promoting Visible-Light Driven Photocatalytic Activity. *Chem. Eur. J.* **2018**, *24*, 7434–7444. [[CrossRef](#)]
42. Yuan, B.; Yang, J.; Song, D.P.; Zuo, X.Z.; Tang, X.W.; Zhu, X.B.; Dai, J.M.; Song, W.H.; Sun, Y.P. Structural, magnetic, and dielectric studies of the Aurivillius compounds $\text{SrBi}_5\text{Ti}_4\text{MnO}_{18}$ and $\text{SrBi}_5\text{Ti}_4\text{Mn}_{0.5}\text{Co}_{0.5}\text{O}_{18}$. *J. Appl. Phys.* **2015**, *117*, 023907. [[CrossRef](#)]
43. Zuo, X.; Zhu, S.; Bai, J.; He, E.; Hui, Z.; Zhang, P.; Song, D.; Song, W.; Yang, J.; Zhu, X.; et al. Enhanced multiferroicity and narrow band gap in B-site Co-doped Aurivillius $\text{Bi}_5\text{FeTi}_3\text{O}_{15}$. *Ceram. Int.* **2019**, *45*, 137–143. [[CrossRef](#)]
44. Wanger, C.D.; Riggs, W.M.; Davis, L.E.; Moulder, J.F.; Muilenberg, G.E. *Handbook of X-ray Photoelectron Spectroscopy*; Perkin-Elmer Corp., Physical Electronics Division: Eden Prairie, MN, USA, 1979; 190p.
45. Song, D.; Zuo, X.; Yuan, B.; Tang, X.; Song, W.; Yang, J.; Zhu, X.; Sun, Y. Enhanced remnant polarization in ferroelectric $\text{Bi}_6\text{Fe}_2\text{Ti}_3\text{O}_{18}$ thin films. *CrystEngComm* **2015**, *17*, 1609–1614. [[CrossRef](#)]
46. Liu, X.; Xu, L.; Huang, Y.; Qin, C.; Qin, L.; Seo, H.J. Improved photochemical properties of Aurivillius $\text{Bi}_5\text{Ti}_3\text{FeO}_{15}$ with partial substitution of Ti^{4+} with Fe^{3+} . *Ceram. Int.* **2017**, *43*, 12372–12380. [[CrossRef](#)]
47. Sanjinés, R.; Tang, H.; Berger, H.; Gozzo, F.; Margaritondo, G.; Lévy, F. Electronic structure of anatase TiO_2 oxide. *J. Appl. Phys.* **1994**, *75*, 2945. [[CrossRef](#)]
48. Bertóti, I.; Mohai, M.; Sullivan, J.L.; Saied, S.O. Surface characterisation of plasma-nitrided titanium: An XPS study. *Appl. Surf. Sci.* **1995**, *84*, 357–371. [[CrossRef](#)]
49. Bharti, B.; Kumar, S.; Lee, H.N.; Kumar, R. Formation of oxygen vacancies and Ti^{3+} state in TiO_2 thin film and enhanced optical properties by air plasma treatment. *Sci. Rep.* **2016**, *6*, 32355. [[CrossRef](#)]
50. Di Mo, S.; Ching, W.Y. Electronic and optical properties of three phases of titanium dioxide: Rutile, anatase, and brookite. *Phys. Rev. B* **1995**, *51*, 13023–13032.
51. Li, X.; Ju, Z.; Li, F.; Huang, Y.; Xie, Y.; Fu, Z.; Knize, R.J.; Lu, Y. Visible light responsive $\text{Bi}_7\text{Fe}_3\text{Ti}_3\text{O}_{21}$ nanoshelf photocatalysts with ferroelectricity and ferromagnetism. *J. Mater. Chem. A* **2014**, *2*, 13366–13372. [[CrossRef](#)]
52. Urbach, F. The long-wavelength edge of photographic sensitivity and of the electronic Absorption of Solids. *Phys. Rev.* **1953**, *92*, 1324. [[CrossRef](#)]
53. Ilican, S.; Caglar, Y.; Caglar, M.; Kundakci, M.; Ates, A. Photovoltaic solar cell properties of $\text{Cd}_x\text{Zn}_{1-x}\text{O}$ films prepared by sol-gel method. *Int. J. Hydrog. Energy* **2009**, *34*, 5201–5207. [[CrossRef](#)]
54. Bai, W.; Xu, W.F.; Wu, J.; Zhu, J.Y.; Chen, G.; Yang, J.; Lin, T.; Meng, X.J.; Tang, X.D.; Chu, J.H. Investigations on electrical, magnetic and optical behaviors of five-layered Aurivillius $\text{Bi}_6\text{Ti}_3\text{Fe}_2\text{O}_{18}$ polycrystalline films. *Thin Solid Films* **2012**, *525*, 195–199. [[CrossRef](#)]
55. Choudhury, B.; Choudhury, A. Oxygen defect dependent variation of band gap, Urbach energy and luminescence property of anatase, anatase-rutile mixed phase and of rutile phases of TiO_2 nanoparticles. *Phys. E Low-Dimens. Syst. Nanostruct.* **2014**, *56*, 364–371. [[CrossRef](#)]
56. Kim, S.; Ko, K.C.; Lee, J.Y.; Illas, F. Single oxygen vacancies of $(\text{TiO}_2)_{35}$ as a prototype reduced nanoparticle: Implication for photocatalytic activity. *Phys. Chem. Chem. Phys.* **2016**, *18*, 23755–23762. [[CrossRef](#)]
57. Ouyang, B.; Zhang, K.; Yang, Y. Photocurrent Polarity Controlled by Light Wavelength in Self-Powered ZnO Nanowires/ SnS Photodetector System. *IScience* **2018**, *1*, 16–23. [[CrossRef](#)]
58. Morgan, B.J.; Watson, G.W. Intrinsic n-type defect formation in TiO_2 : A comparison of rutile and anatase from GGA+U calculations. *J. Phys. Chem. C* **2010**, *114*, 2321–2328. [[CrossRef](#)]
59. Takahashi, M.; Noguchi, Y.; Miyayama, M. Electrical conduction mechanism in $\text{Bi}_4\text{Ti}_3\text{O}_{12}$ single crystal. *Jpn. J. Appl. Phys. Part 1 Regul. Pap. Short Notes Rev. Pap.* **2002**, *41*, 7053–7056. [[CrossRef](#)]
60. Long, M.; Cai, W.; Cai, J.; Zhou, B.; Chai, X.; Wu, Y. Efficient photocatalytic degradation of phenol over $\text{Co}_3\text{O}_4/\text{BiVO}_4$ composite under visible light irradiation. *J. Phys. Chem. B* **2006**, *110*, 20211–20216. [[CrossRef](#)]

Publisher's Note: MDPI stays neutral with regard to jurisdictional claims in published maps and institutional affiliations.



© 2020 by the authors. Licensee MDPI, Basel, Switzerland. This article is an open access article distributed under the terms and conditions of the Creative Commons Attribution (CC BY) license (<http://creativecommons.org/licenses/by/4.0/>).